

Second harmonic microscopy to quantify renal interstitial fibrosis and arterial remodeling

Mathias Strupler

CNRS
Ecole Polytechnique
Laboratoire d'Optique et Biosciences
91128 Palaiseau France
and
Institut National de la Santé et de la Recherche Médicale
INSERM U696
91128 Palaiseau, France

Monica Hernest

CNRS
Ecole Polytechnique
Laboratoire d'Optique et Biosciences
91128 Palaiseau, France
and
Institut National de la Santé et de la Recherche Médicale
INSERM U696
91128 Palaiseau, France
and
Cardiovascular Research Center Inserm Lariboisière
Institut National de la Santé et de la Recherche Médicale
INSERM U689
75010 Paris, France

Cécile Fligny

Cardiovascular Research Center Inserm Lariboisière
Institut National de la Santé et de la Recherche Médicale
INSERM U689
75010 Paris, France

Jean-Louis Martin

CNRS
Ecole Polytechnique
Laboratoire d'Optique et Biosciences
91128 Palaiseau, France
and
Institut National de la Santé et de la Recherche Médicale
INSERM U696
91128 Palaiseau, France

Pierre-Louis Tharoux

Cardiovascular Research Center Inserm Lariboisière
Institut National de la Santé et de la Recherche Médicale
INSERM U689, 75010 Paris, France

Marie-Claire Schanne-Klein

CNRS
Laboratoire d'Optique et Biosciences
91128 Palaiseau, France
and
Institut National de la Santé et de la Recherche Médicale
INSERM U696
91128 Palaiseau, France

1 Introduction

The progression of chronic renal failure is relentless in the majority of patients with chronic nephropathies. The extent of

Abstract. Interstitial fibrosis is a powerful pejorative predictor of progression of nephropathies in a variety of chronic renal diseases. It is characterized by the depletion of kidney cells and their replacement by extracellular matrix, in particular, type-I fibrillar collagen, a protein scarce in normal interstitium. However, assessment of fibrosis remains a challenge in research and clinical pathology. We develop a novel methodology based on second harmonic generation (SHG) microscopy, and we image collagen fibers in human and mouse unstained kidneys. We take into account the variability in renal shape, and we develop automated image processing for quantitative scoring of thick murine tissues. This approach allows quantitative 3-D imaging of interstitial fibrosis and arterial remodeling with high accuracy. Moreover, SHG microscopy helps to raise pathophysiological questions. First, imaging of a large volume within a mouse kidney shows that progression of fibrosis is a heterogeneous process throughout the different renal compartments. Second, SHG from fibrillar collagens does not overlap with the glomerular tuft, despite patent clinical and experimental glomerulosclerosis. Since glomerulosclerosis involves SHG-silent nonfibrillar collagens, our work supports pathophysiological differences between interstitial fibrosis and glomerulosclerosis, a clearly nonfibrotic process. © 2008 Society of Photo-Optical Instrumentation Engineers. [DOI: 10.1117/1.2981830]

Keywords: fibrosis; collagen; hypertension; kidney; angiotensin; multiphoton microscopy; second harmonic generation; vascular remodeling.

Paper 08099R received Mar. 21, 2008; revised manuscript received Jun. 16, 2008; accepted for publication Jun. 16, 2008; published online Oct. 14, 2008.

tubulointerstitial fibrosis correlates best with the deterioration in glomerular filtration rate in all kidney diseases including hypertensive nephropathy (HN).¹⁻⁴ This is due to the underlying scarring process characterized by the depletion of kidney cells and their replacement by extracellular matrix (ECM), in particular by type-I fibrillar collagen.⁵ Normal kid-

Address all correspondence to Marie-Claire, Schanne-Klein, Laboratory for Optics and Biosciences, Ecole Polytechnique, Route de Saclay, Palaiseau, cedex 91128 France; Tel: +33 (0) 169 33 50 60; Fax: +33 (0) 169 33 50 84; E-mail: Marie-Claire.Schanne-Klein@polytechnique.fr

ney structures express very little collagen I in the interstitium and glomeruli, whereas renal and extrarenal arteries constitutively express adventitial collagen I. Although most investigations on HN have focused on the glomerulus and renal microvasculature, tubulointerstitial injury is also a major feature of HN, and remains an important predictor of renal dysfunction. This is striking because HN is generally attributed to increased mechanical stress of the vasculature, which may explain vascular adaptive fibrosis similar to that observed in extrarenal arteries, but may not explain the heterogeneous spreading of tubulointerstitial fibrosis. In addition, several recent experimental and clinical studies provided evidence that tubular epithelial cells can undergo phenotypic change, acquiring myofibroblast-like features such as α smooth muscle actin expression, loss of cytokeratin, and de novo fibrillar collagen I and III expression,⁶ thereby undergoing epithelial-mesenchymal-transition (EMT).^{7,8} Thus, several potential cell types may promote interstitial fibrosis, and it is therefore crucial to develop tools to understand where collagen fibers originate and accumulate in the kidney during pathologies.

Two bottlenecks have impaired efforts of investigators to quantify and locate kidney fibrosis. First, interstitial collagen fibrils form elaborate 3-D arrays that extend over micrometers to millimeters. These 3-D networks are therefore hardly quantified by contrast with ECM accumulation in well-defined structures such as glomeruli and vessels sections. Second, conventional histological staining techniques (hematoxylin and eosin, periodic acid Schiff or Masson's trichrome stains) are not specific to fibrillar collagen. Specificity is improved using picosirius red with polarized light⁹ or immunohistochemical labeling; however, these techniques lack 3-D resolution. In addition, since assessment of the fibrillar collagen is heavily dependent on the thickness of histological sections and the yield of staining, conventional stains lack reproducibility for quantitative purposes. For instance, evaluation of interstitial fibrosis during chronic allograft nephropathy is the most inconsistent index in the Banff score, which is the standardized classification of allograft pathology.¹⁰

In this context, we propose to take advantage of intrinsic second harmonic generation (SHG) from fibrillar collagens. SHG is a multiphoton process where an intense impulsive laser source, at frequency ω , induces a second-order nonlinear polarization in the sample under study, which coherently radiates at the harmonic frequency 2ω . SHG signals are therefore detected at exactly half the excitation wavelength, whereas two-photon excited fluorescence (2PEF) signals are red-shifted compared to the SHG frequency. SHG from collagen fibers was first reported in the 1980's in a rat-tail tendon¹¹ and then utilized in multiphoton microscopy in combination with 2PEF¹²⁻²⁵ and third-harmonic generation²⁶ to visualize the 3-D morphology of thick unstained tissues. We recently showed that SHG microscopy presents unique advantages compared to conventional optical techniques for quantitative 3-D imaging of fibrillar collagen.²² First, SHG microscopy is a specific structural probe for *fibrillar* collagen, and no SHG signal is obtained from type-IV *nonfibrillar* collagen in tissues.^{22,27} The high specificity of SHG signals from fibrillar collagen results in a small background noise in SHG images, enabling sensitive and quantitative measurements of the extent of the fibrillar network. Reproducibility of these measurements is furthermore ensured by the absence of any stain-

ing or labeling. Second, SHG microscopy is a versatile technique: it does not require any preparation of the tissue and is applicable to fresh, frozen, or fixed tissues (including alcoholic fixation or paraffin embedding).²¹ Third, SHG microscopy presents intrinsic 3-D resolution due to its multiphoton character. It is thus insensitive to mild thickness variations in fixed or frozen sections. Most importantly, SHG microscopy is robust upon light scattering within tissues, and enables improved depth penetration within tissues compared to confocal microscopy.

In the present study, we demonstrate that SHG microscopy is a valuable tool for the investigation of heterogeneous accumulation of fibrillar collagen during experimental hypertensive renal fibrosis and human chronic allograft nephropathy, and permits the precise measurement of hypertensive vascular remodeling at the micrometer scale. Furthermore, SHG microscopy allows us to improve the characterization of the hypertensive renal fibrosis induced by Angiotensin II (AngII) in mice and to unravel the spatiotemporal progression of fibrosis in the different renal compartments.

2 Materials and Methods

2.1 Biopsy Protocol

Human kidney samples were collected from transplant recipients with stable graft function 3 months after engraftment of kidney from a deceased donor. Transplantations were performed at Hôpital Tenon, Paris, France. Needle-core biopsies were obtained using a biopsy gun (Monopty Bard, Covington, United Kingdom) with a 16-gauge needle.

2.2 Models of Angiotensin-II-Induced Hypertension and Crescentic Glomerulonephritis

We studied male mice aged 8 to 14 weeks with similar genetic background (C57BL/6J background). Baseline blood pressure measurements were performed on five consecutive days. After these baseline recordings, an osmotic minipump (Alzet Model 2004; Durect, California) infusing AngII (Sigma, Saint Louis, Missouri) at a rate of 1 $\mu\text{g}/\text{kg}/\text{min}$ was implanted subcutaneous for 28 days as described by Crowley et al.²⁸ Blood pressure was regularly monitored to verify continuous hypertension. In a subset of experiments, a second osmotic minipump was implanted on day 27 to ensure AngII-infusion up to day 49. The animals ingested a normal diet containing 5% sodium chloride (SDS-Dietex, France) to accentuate hypertension and kidney injury. We also used the accelerated antiglomerular basement membrane anti(GBM) crescentic glomerulonephritis (GN) model, as described by Lloyd et al.²⁹ Briefly, mice were given subcutaneous injections of 200- μg normal sheep IgG [100 μl into each flank of normal sheep IgG (Sigma) diluted to 1 mg/ml in a solution of 50% Freund's complete adjuvant and 50% saline]. Six days later (day 1), GN was induced by intravenous injection of sheep anti-GBM serum. Serum injections were repeated daily on days 2 and 3. The protocols followed the French Department of Agriculture and the National Institute of Health guidelines for animal care and protection.

2.3 Histopathological Analysis

Human kidney biopsies specimens were fixed in formaldehyde. After fixation, tissues were dehydrated with a graded series of ethanol and xylene, embedded in paraffin, and cut into 10- μm sections for SHG analysis.

Following 28 or 49 days of AngII infusion or 17 days after anti-GBM serum administration in C57BL6/J mice, murine kidneys were harvested and weighed. One half of a kidney was fixed in formalin, embedded in paraffin, sectioned (3 μm), and stained with Masson's trichrome. All of the tissues were examined by a pathologist without knowledge of treatment groups. The pathological abnormalities were graded based on the presence and severity of component abnormalities, including glomerulosclerosis. Grading for glomerulosclerosis was performed using a semiquantitative scale as previously described.³⁰ Percent glomerulosclerosis was defined as the number of glomeruli with evidence of sclerosis divided by the total number of glomeruli in the section. For tubulointerstitial areas, individual scores adapted from Spurney et al.³¹ were obtained for the severity of interstitial inflammatory cell infiltrates and severity of tubular atrophy. The second half of the kidney was fixed in phosphate buffered saline (PBS) buffered 4% formaldehyde and used for multiphoton microscopy. 200- μm -thick coronal slices were cut using a vibrating-blade microtome (VT1000S, Leica, Germany) at 25% of the kidney height.

2.4 Multiphoton Microscopy

Multiphoton images were recorded using a custom-built upright laser scanning microscope, as previously described.²² Briefly, SHG and 2PEF signals were simultaneously excited by a femtosecond titanium-sapphire laser adjusted to 860 nm (Tsunami, Spectra-Physics, Irvine, California), and dispatched to two photon-counting epidection channels using a dichroic mirror (FF458-Di01, Semrock, Rochester, New York) and appropriate spectral filters (E700SP and GG455 in the 2PEF channel, E700SP and HQ430/20 in the SHG channel, Chroma, Rockingham, Vermont). Alternatively, the SHG signal from thin biopsies was detected in the forward direction using the same filters. We used circular polarization to minimize orientation effects in the image plane, similarly to circularly polarized Picosirius imaging.⁹

Visualization of micrometer or submicrometer collagen fibers that were heterogeneously distributed in the kidney tissue at millimeter scale required both a large field of view and a good spatial resolution. We therefore used a 20 \times 0.95-NA objective lens (Olympus, Japan) with 512 \times 512- μm^2 field of view and 0.40- μm (lateral) \times 1.6- μm (axial) resolution near the sample surface. Furthermore, we scanned the tissue using a motorized stage with 12-mm travel range. We always scanned 2.5 \times 5-mm² areas with 0.8 \times 0.8- μm^2 pixel size, at 100-kHz pixel rate and 50-mW excitation, and we acquired eight images spaced out 5 μm apart within the depth of the tissue. Voxel size was set to a slightly greater value than the optical resolution near the sample surface to restrain imaging time to typically 90 min per sample. Nevertheless, images acquired for 3-D reconstructions were recorded with 0.4 \times 0.4- μm^2 pixel size and were spaced out 0.5 μm apart within the tissue.

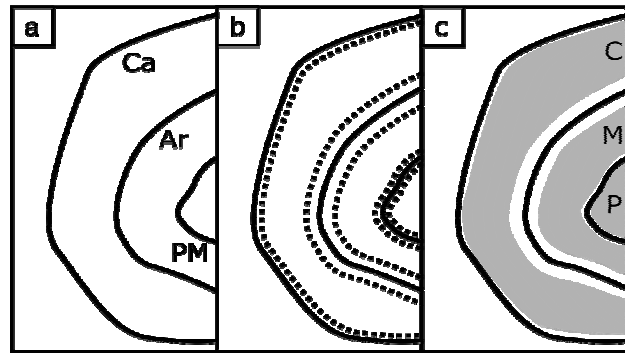


Fig. 1 Segmentation procedure. (a) Plot of three curves underlining morphological key features of the kidney: Ca, along the capsule, Ar, through the arteries centers, and PM at the edge of medulla and papilla. (b) Dilation or contraction of these curves, using elliptical fitting to define a reference center, to exclude the region of the arcuate arteries and the borderline regions. (c) Location of the three regions for SHG scoring: the cortex region [C] between Ca-40 μm and Ar+160 μm , the medulla region [M] between Ar-160 μm and PM+40 μm , and the papilla region [P] limited by PM+40 μm .

2.5 Second Harmonic Generation Image Processing and Segmentation

Stacks of SHG and 2PEF images were combined and processed using an algorithm developed to enhance the fiber contrast, as previously described.²² 3-D reconstructions were performed using Amira (Mercury Computer Systems, Chelmsford, Massachusetts). Fibrosis scores were obtained from SHG data using a phenomenological approach as previously published:²² they were calculated as the volume density of voxels exhibiting significant SHG signal in the image stack.

To take into account the specific morphology of every murine kidney, that is the variability in kidney shape and in radial location of the arteries, we developed a segmentation algorithm and calculated fibrosis scores on distinct morphological regions of the kidney. We first manually outlined the capsule and the papilla in every SHG/2PEF image, and selected the centers of the arcuate arteries in the cortico-medullary area. Our algorithm then yielded three curves: Ca, along the capsule, Ar, through the arterial centers, and PM, at the edge of medulla and papilla [see Fig. 1(a)]. These curves were fitted to ellipses, enabling their dilation or contraction toward the center of the ellipse, as shown in Fig. 1(b). Three regions were defined by our algorithm [Fig. 1(c)]: the outer cortical region [C] between Ca-40 μm and Ar+160 μm , the medulla region [M] between Ar-160 μm and PM+40 μm , and the papilla region [P] limited by PM-40 μm . The contraction of Ca by 40 μm ensures that large SHG signals from the capsule do not contribute to the cortical SHG score. The ± 160 - μm shift of the Ar curve apart from the artery centers aims at excluding the arteries from any SHG scoring, because their quantity and size in every kidney sample show large fluctuations (see results). The ± 40 - μm replicas of MP minimizes the uncertainty of the borderline position between the medulla and the papilla. Our algorithm finally provided SHG scores for all these regions, which were calculated as the percentage of nonzero SHG voxels averaged over the 40- μm z stack.

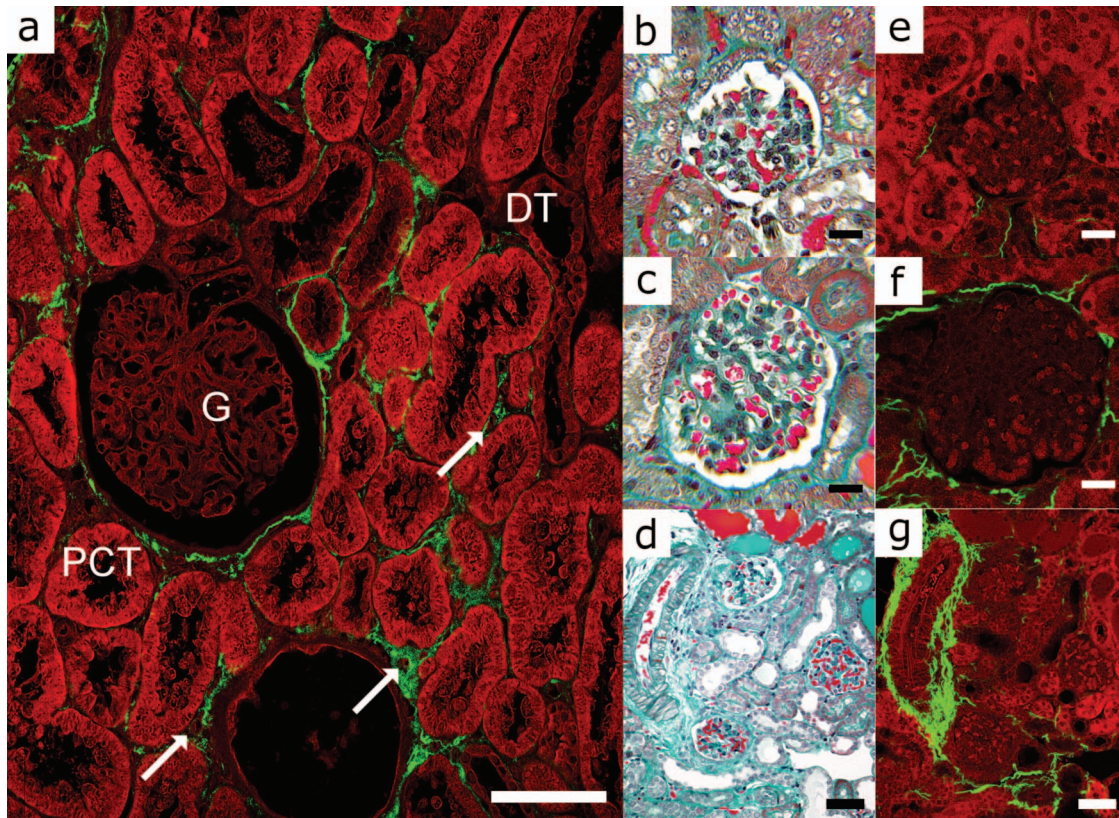


Fig. 2 SHG microscopy versus histological staining of kidney cortex. (a) Multiphoton image of an unstained human renal implantation biopsy: SHG (green color) reveals collagen fibers in the Bowman's capsule and the tubular interstitium, and endogenous 2PEF (red color) underlines tubules, glomeruli, and arterioles. PCT: proximal convoluted tubules, DT: distal tubules, G: glomerulus, white arrows: arterioles. (b) and (c) Histological versus (d) and (e) multiphoton images [same color code as for (a)] of serial renal sections of control mouse (b) and (d) and hypertensive mouse infused with AngII for 28 days (c) and (e). Note that hypertension promoted the accumulation of nonfibrillar extracellular matrix within the glomerular tuft stained with Masson's trichrome (c) [SHG silent in (f)] and the accumulation of fibrillar collagen in the Bowman's capsule and the surrounding interstitium, similarly to the observation in the human biopsy in (a). Scale bars: (a) 100 μm , (b), (c), (e), and (f) 20 μm and (d) and (g) 50 μm .

2.6 Quantitative Analysis of the Arcuate Artery Hypertensive Remodeling

We performed a quantitative analysis of the morphology of arcuate arteries. For every mouse, we selected one to five arteries. Their section was approximately elliptical because their orientation in the tissue was not absolutely perpendicular to the image plane. We considered only the small axis of the ellipse, which was not distorted by the 2-D sectioning, and measured: 1. the lumen radius L , as delineated by 2PEF from the internal elastic lamina; 2. the thickness of the media (region exhibiting 2PEF) M ; and 3. the thickness of the adventitia (region exhibiting SHG) A . The measured artery radii ($L+M+A$) ranged from 21 to 84 μm (average: 40 μm). The mean cross sectional area (CSA) was calculated for each experimental condition. We normalized the data with respect to the media outer radius ($L+M$) for every artery to compare the morphology of arteries having different sizes. We then calculated mean values of the raw data (in μm) and of the normalized dimensions (in %) for every mouse. The results were averaged within the three groups: the control mice ($n=7$), the 28 days-infused mice ($n=7$), and the 49 days-infused mice ($n=7$). The same method was used for the calculation of the media to lumen (M/L) and wall to lumen [$(A+M)/L$] ratios.

2.7 Statistical Methods

The values for each parameter within a group were expressed as the mean \pm the standard error of the mean (SEM). For comparisons between groups, a one-way nonparametric Kruskal-Wallis test was employed followed by Dunn's Multiple Comparison test (Prism 5, GraphPad Software Incorporated, San Diego, California). For comparison of different measurements performed on the same group, we used the Kendall tau coefficient.

3 Results

3.1 Multiphoton Images of Human and Murine Renal Sections

We first studied human renal biopsies removed three months after renal transplant to assess interstitial fibrosis. Figure 2(a) shows a multiphoton image of an unstained formalin-fixed paraffin-embedded section: SHG and 2PEF contrasts were recorded simultaneously and displayed with green and red colors, respectively, in the combined image. 2PEF from endogenous cellular chromophores revealed tubules, glomeruli, and arterioles. SHG revealed collagen fibers in the Bowman's capsule and in the tubular interstitium. We also observed

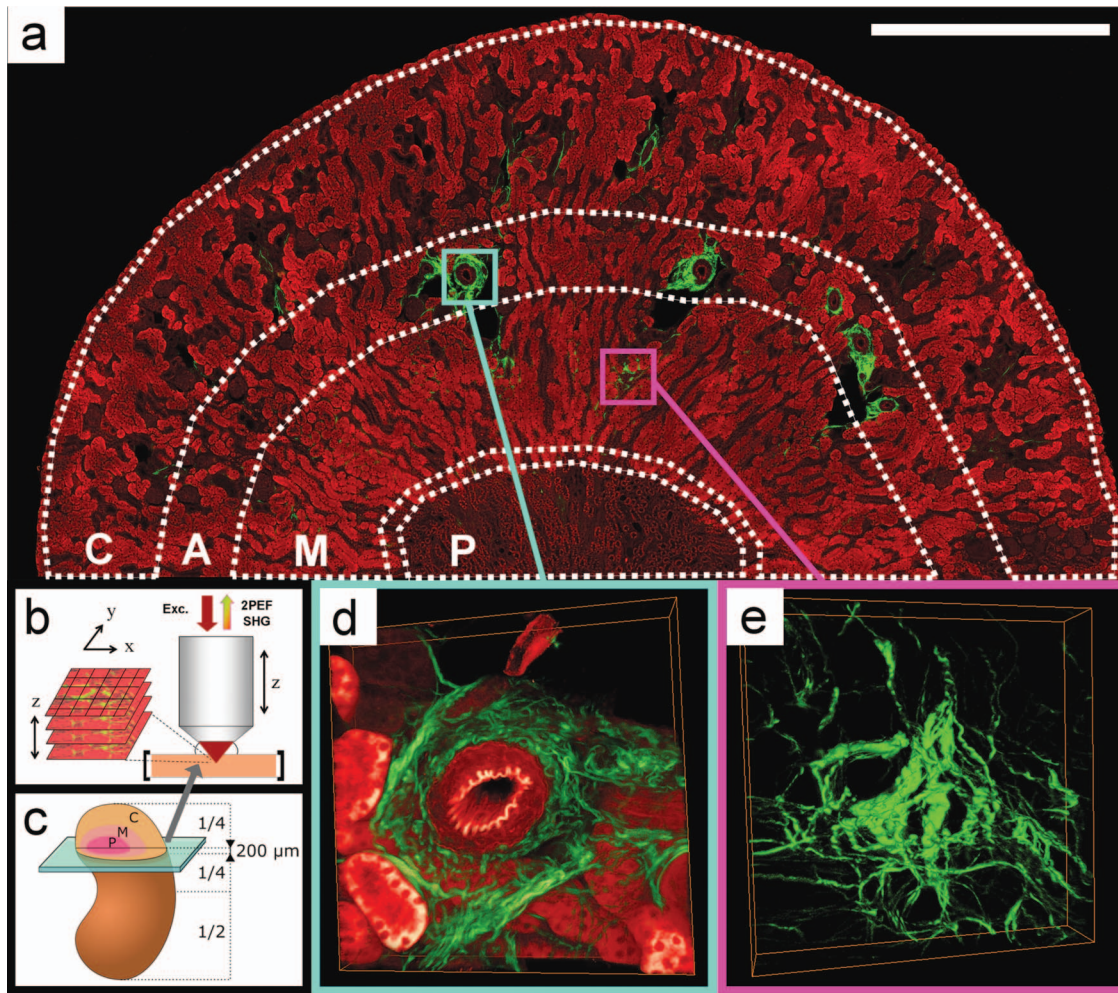


Fig. 3 Multiphoton images of fibrotic murine kidney tissue. (a) Multiphoton image of a representative coronal renal section from a 49 days-AngII infused mouse showing renal papilla (P), medulla (M), outer cortex (C), and arcuate arteries (A) along the boundary between cortex and medulla. SHG (green color) reveals collagen fibers in the tubular interstitium and in the arterial adventitia, and 2PEF (red color) underlines tubules. This $4.8 \times 2.4\text{-mm}^2$ image is obtained by stitching 10×20 laser scanned images (dimension: $270 \times 270 \mu\text{m}^2$, pixel size: $0.8 \times 0.8 \mu\text{m}^2$) acquired sequentially by moving the kidney sample with a motorized microscope stage. Scale bar: $500 \mu\text{m}$. The dotted white lines underline segmentation used for SHG scoring (excluding the artery region and the borders). (b) Scheme of the laser scanning multiphoton microscope showing epidetection of z stacks of SHG/2PEF images. (c) Scheme of the kidney coronal slicing for multiphoton microscopy. (d) and (e) 3-D reconstructions of underlined areas in (a) ($270 \times 270 \times 40 \mu\text{m}^3$ with $0.4 \times 0.4 \times 1\text{-}\mu\text{m}^3$ voxel size), showing (d) an arcuate artery and (e) interstitial fibrosis. The artery morphology in (d) is revealed by 2PEF (red color) obtained from elastin in the internal lamina and from cellular chromophores in the media, and by SHG (green color) from collagen fibers in the adventitia. Enhanced SHG contrast in (e) underlines the 3-D distribution of collagen fibers around arterioles and tubules (no 2PEF displayed here).

small fluorescent structures surrounded by collagen fibers in the interstitium, consistent with capillary morphology.

To study the progression of interstitial fibrosis and to compare the features of mouse renal fibrosis with human renal fibrosis, we used a well-characterized animal model of hypertensive renal fibrosis.²⁸ C57B16 mice were infused for 28 days with AngII, and they developed increased systolic blood pressure, albuminuria (data not shown), and glomerulosclerosis compared with normotensive counterparts, as evidenced by Masson's trichrome staining [Figs. 2(b)–2(d)]. Serial sections of kidney cortex from the same control and hypertensive mice were visualized using multiphoton microscopy [Figs. 2(e)–2(g)]. Multiphoton images of representative sclerosed glomeruli [Figs. 2(f) and 2(g)] showed numerous collagen fibers in the Bowman's capsule and in the tubular

interstitium, whereas the control unstained section [Fig. 2(e)] showed no SHG signal, thus no fibrillar collagen accumulation, except for a few thin fibers in the tubular interstitium. Notably, as in human kidneys [Fig. 2(a)], collagen fibers were never observed within the glomerular tuft despite patent glomerulosclerosis after chronic and severe hypertension [Figs. 2(f) and 2(g)].

3.2 Three-Dimensional Distribution of Collagen Fibers in Murine Fibrotic Kidney Tissue

To characterize the collagen distribution on a large scale, we imaged renal cortex and medulla in thick coronal slices [Figs. 3(a)–3(c)]. Figure 3(a) shows a combined SHG/2PEF image from a 49 day-infused mouse obtained by stitching many im-

Table 1 Dimensions of arcuate arteries in control and hypertensive mice. Mean values and standard errors of the mean of the arcuate artery dimensions for control mice versus 28- and 49-days AngII-infused mice. Raw values are directly obtained from length measurements, as schematized in Fig. 4(a). Normalized values are obtained as the ratio of the raw data to the media outer radius (L+M) in every artery, as explained in the methods. (* $p < 0.05$ versus control value, $n = 7$).

		Control	D28	D49
Vascular size	Artery radius (L+M+A, μm)	40 \pm 3	43 \pm 5	40 \pm 3
	Media radius (L+M, μm)	25 \pm 1	26 \pm 3	24 \pm 2
Cross sectional area	$\pi(L+M)^2$ (μm^2)	2079 \pm 167	2440 \pm 462	2041 \pm 368
Adventitia thickness	Raw value (A, μm)	15 \pm 2	17 \pm 3	15 \pm 2
	Normalized [A/(L+M), %]	58 \pm 8	62 \pm 9	64 \pm 9
Media thickness	Raw value (M, μm)	13 \pm 1	16 \pm 1	16 \pm 2
	Normalized [M/(L+M), %]	52 \pm 3	61 \pm 2	65 \pm 3*
Lumen radius	Raw value (L, μm)	12 \pm 1	11 \pm 2	9 \pm 1
	Normalized [L/(L+M), %]	48 \pm 3	39 \pm 2	35 \pm 3*

ages acquired using an objective with a high numerical aperture. We observed collagen fibers in the adventitia of arcuate arteries and arterioles and in the tubular interstitium.

We also took advantage of the 3-D imaging capability of multiphoton microscopy to visualize the 3-D distribution of collagen fibers in the adventitia from arcuate arteries [Fig. 3(d)] and in the tubular interstitium [Fig. 3(e)]. For this purpose, we reconstructed 3-D images from z stacks of combined SHG/2PEF images. Strong 2PEF signals arose from elastic lamina in the artery media as previously observed^{19,20} [Fig. 3(d)]. As expected, SHG revealed collagen fibers in the vessel adventitia [Fig. 3(d)] and in the tubular interstitium [Fig. 3(e)], where they appeared to form a quasicontinuous network.

3.3 Quantitative Analysis of Arcuate Artery Hypertensive Remodeling

Characterization of the remodeling of resistive arteries in end organs is of major importance in evaluating tissue perfusion, since the peripheral resistance is mainly determined by the distal part of the arterial vasculature (the resistance vessels), consisting of small arteries (diameter $< 300 \mu\text{m}$) and arterioles.^{32,33} Arcuate arteries are less than $50 \mu\text{m}$ in diameter in the mouse kidney, well below the usual threshold of $300 \mu\text{m}$. We focused on these arteries and measured the overall vascular size, the adventitia thickness, the media thickness, and the lumen radius, as shown in Fig. 4(a). Table 1 displays raw and normalized results for control and hypertensive mice. Mean raw data did not present significant changes with hypertension, because of the size heterogeneity of the arteries. However, normalization, taking into account artery radius, revealed a decrease in the lumen radius in hypertensive animals and a concomitant increase of the media thickness. By contrast, we observed no significant change in the adventitia normalized thickness [Fig. 4(b)].

These structural properties of arteries helped determine the physiologically important media to lumen (M/L) and wall to lumen ratios [(M+A)/L] [Figs. 4(c) and 4(d)]. Hypertension significantly increased media to lumen and wall to lumen ratios in these renal resistance arteries. This altered morphology was not associated with any significant increase in the media cross sectional area (Table 1), suggesting rearrangement of the media around a smaller diameter, so-called eutrophic remodeling.³²

3.4 Quantitative Analysis of Segmented Second Harmonic Generation Images Reveals Angiotensin-2-Induced Interstitial Fibrosis in the Cortex

We compared the progression of fibrosis in normal and hypertensive mice infused for 28 or 49 days. Interstitial fibers were heterogeneously distributed in a thin network that accumulated mostly in the inner cortex, close to arcuate arteries, and extended radially in the medulla and in the outer cortex [Figs. 5(a)–5(c)]. Surprisingly, we observed physical connections (or at least very close proximity below the resolution of the microscope) between perivascular, periglomerular, and peritubular fibers. For comparison, we also visualized kidneys from a mouse model of crescentic glomerulonephritis, and we observed a similar distribution of collagen fibers [see Fig. 5(d)].

To discriminate between de novo interstitial fibrosis and constitutive adventitial collagen around arcuate arteries, we performed a radial segmentation of SHG images excluding arcuate arteries as well as border regions, and selected outer-cortical, medullar, and papillary regions [see white dotted line in Figs. 3(c) and 5]. We then obtained fibrosis scores in various anatomical regions from the kidney tissue by measuring the density of voxels exhibiting nonzero SHG signal.

Averaged values of the cortical scores and of the total scores are shown in Fig. 6 for control and hypertensive mice.

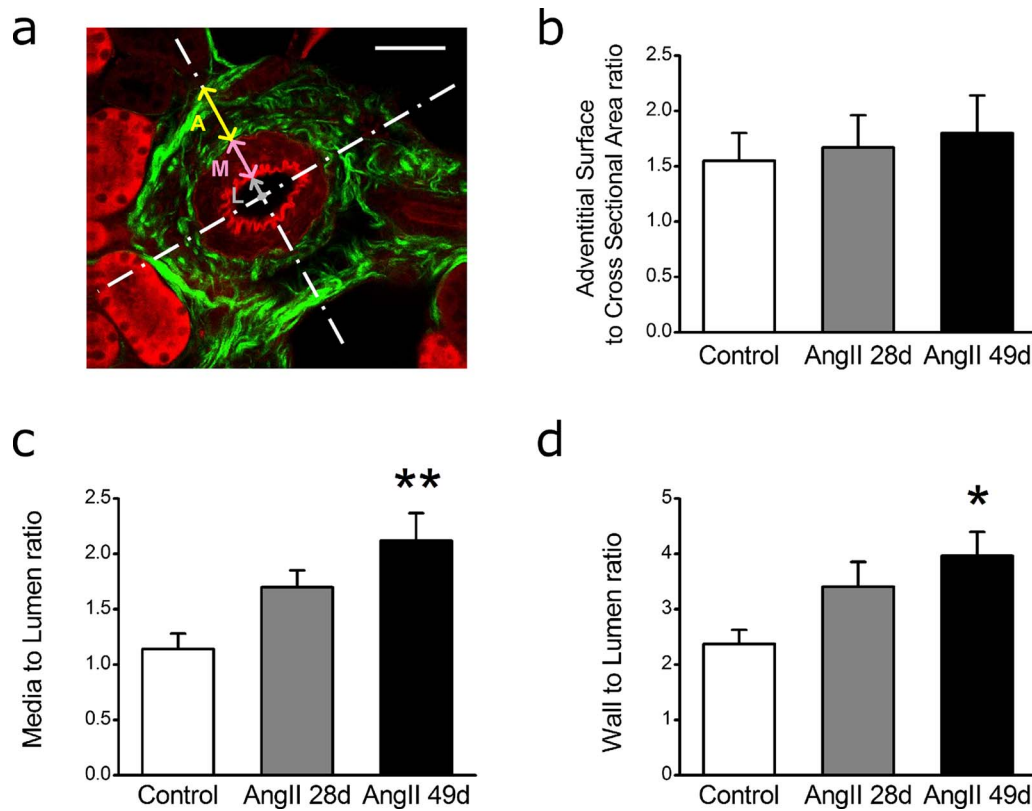


Fig. 4 Quantitative analysis of arcuate artery remodeling in hypertensive animals. (a) Multiphoton 2-D image of the same artery as in Fig. 2(d). Measurements performed along the small nondistorted axis are schematized by double arrows: A=adventitia thickness, M=media thickness, L=lumen radius, and A+M=wall thickness. Scale bar: 50 μm . (b) Stability of adventitia surface normalized to cross sectional area in 28 and 49-day AngII-infused mice versus control mice. (c) Increase in media to lumen ratio (M/L) in 28 and 49-day AngII-infused mice versus control mice. (d) Increase in wall to lumen ratio [(A+M)/L] in 28 and 49-day AngII-infused mice versus control mice. (* $p < 0.05$ versus control, ** $p < 0.01$ versus control, $n = 7$ per condition.)

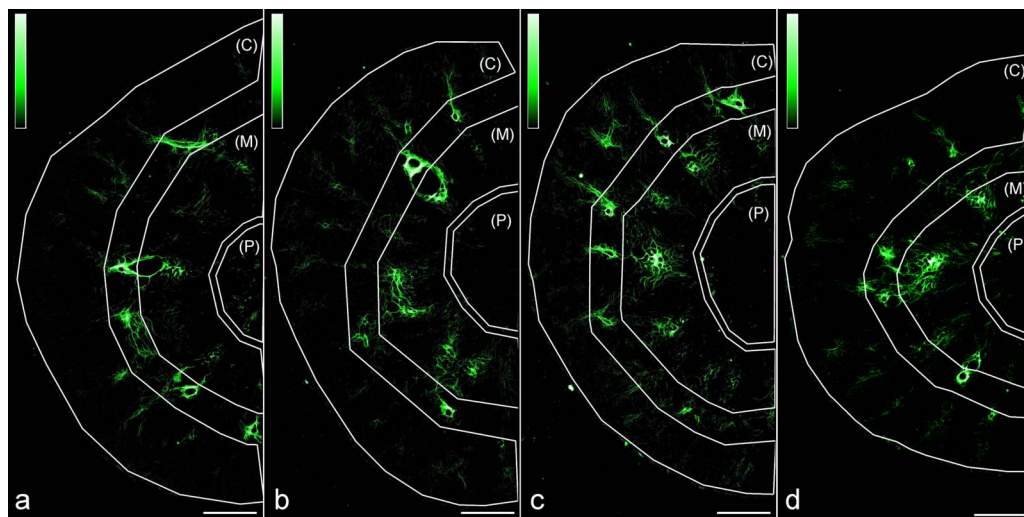


Fig. 5 SHG imaging of renal fibrosis. SHG density images of coronal renal slices from representative (a) 0, (b) 28, and (c) 49 day-AngII-infused mice and (d) GN mouse, giving the percentage of voxels above the threshold over the 40- μm z stack (black=0% to white=100%). Scale bar: 500 μm . The white lines underline segmentation used for SHG scoring (excluding the artery region and the borders): (C) (cortex), (M) medulla, and (P) papilla. Mean value of the SHG scores calculated on these regions are the following: (a) D0 mouse: (C) 0.31%, (M) 0.85%, (P) 0.49%; (b) D28 mouse: (C) 0.42%, (M) 2.13%, (P) 0.11%; (c) D49 mouse: (C) 0.74%, (M) 1.83%, (P) 0.20%; and (d) GN model: (C) 0.41%, (M) 2.79%, (P) 0.29%.

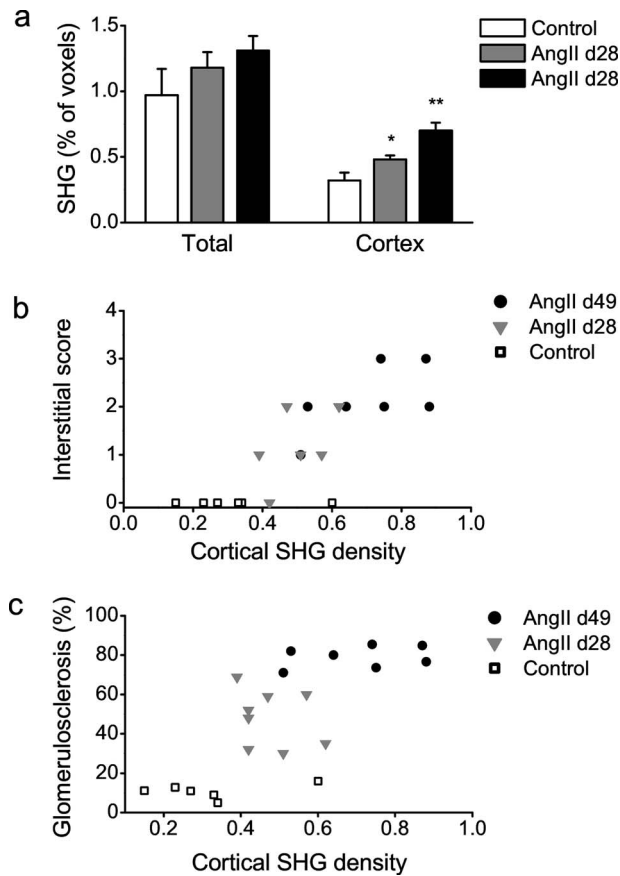


Fig. 6 Quantitative scoring of renal fibrosis. (a) Mean values of SHG scores calculated in the whole SHG images and in cortical areas for six control mice (white triangles) versus AngII-infused mice for 28 days (gray diamond) and 49 days (black circle). Errors bars correspond to standard errors of the mean. The cortical score shows smaller absolute values but larger differences on AngII-induced hypertension. (* $p < 0.05$ versus control; ** $p < 0.01$ versus control; $n = 6$ to 8 per condition). (b) Automated cortical SHG score plotted as a function of a semiquantitative estimate of interstitial damage for control and hypertensive mice ($\tau = 0.68, p < 0.01$). (c) Glomerulosclerosis index versus cortical SHG score for control and hypertensive mice ($\tau = 0.55, p < 0.01$).

Both scores increased for infused mice, and with the infusion duration. Cortical scores showed the larger relative increase in hypertensive kidneys. Medullary scores were highly heterogeneous in control kidneys and showed no significant change with hypertension (data not shown). Papillary SHG signals were scarce, with low signal over noise ratios and unreliable SHG scores.

Finally, we confronted cortical SHG scores with usual histopathological methods that evaluate kidney damages in Masson's trichrome stained sections. We plotted cortical SHG scores as a function of histopathological evaluation of interstitial damage and inflammation [Fig. 6(b)] and glomerulosclerosis scores [Fig. 6(c)] for all mice in the three groups (control, 28-day and 49-day AngII-infused mice, $n = 21$ mice). Semiquantitative histopathological evaluation of interstitial damage and SHG cortical score were found to be correlated ($\tau = 0.68, p < 0.01$) [Fig. 6(b)]. Glomerulosclerosis correlated better with cortical SHG scores ($\tau = 0.55, p$

< 0.01) than with global SHG scores ($\tau = 0.32, p < 0.05$).

4 Discussion

Although the extent of tubulointerstitial fibrosis correlates best with the deterioration in glomerular filtration rate in kidney diseases including hypertensive nephropathy,^{1,3,4} quantification of 3-D arrays of collagen fibers remains a challenge in research and clinical practice. Hypertension is a prominent cause of end-stage renal disease. Yet it is not fully elucidated whether interstitial fibrosis is an early event or not, and where collagen fibers do assemble in the context of causative vascular stress. Combining a mouse model of hypertension and quantitative assessment of the density of SHG signal from collagen fibers, we observed early development of interstitial fibrosis in experimental hypertension with a pattern similar to that observed in human kidney transplants. SHG signal unambiguously evidenced accumulation of collagen fibers in the tubular interstitium and in the Bowman's capsule in the kidneys from hypertensive mice and from patients with chronic renal allograft nephropathy. We also found similar localization of fibers in the interstitium and the Bowman's capsule in a mouse model of crescentic glomerulonephritis, suggesting that common pathways are recruited whatever the cause of the nephropathy.

Conversely, no SHG signal was observed in the glomerulus tuft, indicating that sclerosis of the glomerulus revealed by histological staining is induced by the accumulation of non-fibrillar collagens and other extracellular matrix compounds. Since histological and multiphoton images provide complementary information, combining the two approaches enabled the observation that glomerulosclerosis and renal fibrosis correspond to accumulation of distinct extracellular proteins. Our observation in human and mouse kidneys do not confirm the relevance of numerous reports of procollagen I mRNA expression by glomerular cells *in vitro*, namely mesangial cells,³⁴⁻³⁶ or of high transcriptional activity of an exogenous pro $\alpha 2(I)$ collagen I promoter in glomeruli from hypertensive transgenic mice.³⁷ Furthermore, our findings using SHG microscopy correlate well with immunohistochemical and immunogold labeling studies that led to a similar conclusion in human focal and segmental glomerulosclerosis, membranous glomerulonephritis, and diabetic glomerulopathy.³⁸⁻⁴⁰ Indeed, focal accumulation of collagen type I or III is exceptionally reported and only in severely sclerotic and obsolescent glomeruli.^{41,42} Altogether, our findings suggest strong inhibition of translation of procollagen I mRNAs in glomerular cells *in vivo*. An alternative explanation could be that pathologic glomeruli may produce immunohistochemistry-silent and SHG-silent collagen I that is rapidly degraded or is assembled in a nonfibrillar fashion, an intriguing possibility not yet demonstrated so far, and beyond the scope of the present study.

The relationship between progression of arterial fibrosis and interstitial fibrosis is not well understood so far. High resolution images in kidneys from hypertensive mice showed striking continuity between perivascular, periglomerular, and peritubular fibers. This suggests that hypertensive renal fibrosis results from multiple cellular origins and is unlikely exclusively promoted by periarterial fibrosis or by EMT alone.

Peripheral resistance is determined at the level of the precapillary vessels. The elevated resistance in hypertensive

patients is related to rarefaction (decrease in number of parallel-connected vessels) and narrowing of the lumen of resistance vessels. However, although perfusion of the kidney is a critical determinant of blood pressure regulation, very few quantitative data of remodeling of renal arterioles are available. Our normalized measurements of the arterial sizes demonstrated that the arterial adventitia do not get thicker in AngII-infused mice. This might be due to a lack of sensitivity in the measurement of minor relative changes, since arcuate arteries constitutively exhibit collagen fibers within the adventitia. However, a seven-week regime of severe hypertension that induced significant renal fibrosis and glomerulosclerosis did not affect the geometry of the adventitia of these arteries, otherwise significantly remodeled. The lack of increase of adventitia thickness contrasts with increased accumulation of interstitial fibers. This suggests that the formation of collagen fibers in the arterial adventitia and in the renal interstitium could be regulated by different pathways.

Cross sectional areas remained constant, but with increased media thickness, resulting in a decrease of the lumen radius. This observation is consistent with hypertensive inward eutrophic remodeling found in extrarenal larger arteries, such as in gluteal biopsies from hypertensive subjects and mesenteric arteries from animals that uniformly revealed reduced lumen areas and increased media-lumen ratios without an increase in medial area in resistance vessels.^{32,33,43}

SHG imaging of kidney tissue also revealed high heterogeneity of collagen fibers accumulation. The maximal relative increase of SHG density associated with interstitial fibrosis measured in hypertensive mice was observed in the cortex. However, we observed scarce and thin collagen fibers, and SHG scores in this region rarely exceeded 1%, indicating that less than 1% of the tissue was invaded by collagen fibers. Scanning of large tissue volumes along with automated segmentation and scoring procedures was therefore mandatory to obtain robust data, and proved essential for accurate assessment of fibrosis.

SHG microscopy with automated scanning and image processing produced continuous scores of interstitial fibrosis that were compared with semiquantitative histopathological scoring, taking into account extracellular matrix, tubular damage, and inflammatory infiltrates, all indices being sensitive to pathologist interpretation. As expected, both scoring procedures showed a good correlation, since they measured the nephropathy progression in the same renal compartment. To determine the sensitivity threshold of cortical SHG scores, we also studied female control mice, since females are known to be less prone to fibrosis than males. The averaged cortical SHG score was: 0.16 ± 0.04 ($n=3$) for female control mice, which is smaller than the value obtained for male control mice: 0.32 ± 0.04 ($n=6$). SHG scores therefore appeared to be more sensitive at early stages when Masson's trichrome stained section revealed no apparent damages. Moreover, SHG microscopy could localize fibers and their respective extension and connections.

SHG cortical scores enabled the determination of kidney fibrosis in the same region as that used for measuring conventional glomerulosclerosis scores. Both scores showed good agreement, and we obtained a better correlation than for SHG scores calculated in the whole images. This suggests that partially common mechanisms may promote both processes, at

least in a model of primary vascular injury as in AngII-infused animals.

In conclusion, this study emphasized that renal fibrosis is a markedly heterogeneous process within the kidney. We therefore developed large volume SHG imaging and relevant segmentation of the images, along with automated procedures to ensure high reproducibility and unbiased analysis. Coupling of SHG and 2PEF microscopy also proved to be a precise tool to assess the remodeling of resistive arteries in the kidney. Interestingly, AngII-induced hypertension provoked eutrophic remodeling of arcuate arteries, with no significant increase in the constitutional collagenous adventitia. We found unambiguous evidence of interstitial accumulation of fibrillar collagens in the cortex with no glomerular sclerosis in experimental severe hypertension. This surprising result suggests early onset of interstitial disease, despite causing vascular stress and distinct regulation of collagen fiber deposition in these structures. Since interstitial fibrosis occurs in a wide array of nephropathies, SHG microscopy should help pathological studies and may become a diagnostic and prognostic tool for human tissues.

Acknowledgments

This work was supported by Agence Nationale de la Recherche Grant «Transcola» and by funding from the Institut National de la Santé et de la Recherche Médicale, the Centre National de la Recherche Scientifique, and Ecole Polytechnique. Strupler was supported by a grant from "Région Ile de France." Hernest was supported by a fellowship from the French Ministry for Research and Higher Education. We thank Eric Rondeau for providing us with the human kidney biopsies and Laurent Mesnard for providing us with anti-mouse GBM sheep serum. We acknowledge administrative support from Martine Autran, Laure Lachapelle, and Christelle Français, and technical support from Xavier Solinas and Jean-Marc Sintès. We thank Emmanuel Beaurepaire for the outstanding design of the multiphoton setup.

References

1. K. A. Nath, "Tubulointerstitial changes as a major determinant in the progression of renal damage," *Am. J. Kidney Dis.* **20**, 1–17 (1992).
2. E. C. Bergijk, C. Munaut, J. J. Baelde, F. Prins, J. M. Foidart, P. J. Hoedemaeker, and J. A. Bruijn, "A histologic study of the extracellular matrix during the development of glomerulosclerosis in murine chronic graft-versus-host disease," *Am. J. Pathol.* **140**, 1147–1156 (1992).
3. A. Bohle, G. A. Muller, M. Wehrmann, S. Mackensen-Haen, and J. C. Xiao, "Pathogenesis of chronic renal failure in the primary glomerulopathies, renal vasculopathies, and chronic interstitial nephritides," *Kidney Int.* **49**, S2–9 (1996).
4. A. Bohle, F. Strutz, and G. A. Muller, "On the pathogenesis of chronic renal failure in primary glomerulopathies: a view from the interstitium," *Exp. Nephrol.* **2**, 205–210 (1994).
5. A. A. Eddy, "Molecular basis of renal fibrosis," *Pediatr. Nephrol.* **15**, 290–301 (2000).
6. K. Jinde, D. J. Nikolic-Paterson, X. R. Huang, H. Sakai, K. Kurokawa, R. C. Atkins, and H. Y. Lan, "Tubular phenotypic change in progressive tubulointerstitial fibrosis in human glomerulonephritis," *Am. J. Kidney Dis.* **38**, 761–769 (2001).
7. M. Iwano, D. Plieth, T. M. Danoff, C. Xue, H. Okada, and E. G. Neilson, "Evidence that fibroblasts derive from epithelium during tissue fibrosis," *J. Clin. Invest.* **110**, 341–350 (2002).
8. M. Zeisberg and R. Kalluri, "The role of epithelial-to-mesenchymal transition in renal fibrosis," *J. Mol. Med.* **82**, 175–181 (2004).
9. L. C. U. Junqueira, G. Bignolas, and R. R. Brentani, "Picrosirius

- staining plus polarization microscopy, a specific method for collagen detection in tissue sections," *Histochem. J.* **11**, 447–4155 (1979).
10. P. C. Grimm, P. Nickerson, J. Gough, R. Mckenna, E. Stern, and D. N. Rush, "Computerized image analysis of Sirius Red-stained renal allograft biopsies as a surrogate marker to predict longterm allograft function," *J. Am. Soc. Nephrol.* **14**, 1662–1668 (2003).
 11. I. Freund, M. Deutsch, and A. Sprecher, "Optical second-harmonic microscopy, crossed-beam summation and small-angle scattering in rat-tail tendon," *Biophys. J.* **50**, 693–712 (1986).
 12. P. J. Campagnola, A. C. Millard, M. Terasaki, P. E. Hoppe, C. J. Malone, and W. A. Mohler, "Three-dimensional high-resolution second-harmonic generation imaging of endogenous structural proteins in biological tissues," *Biophys. J.* **82**, 493–508 (2002).
 13. A. Zoumi, A. Yeh, and B. J. Tromberg, "Imaging cells and extracellular matrix *in vivo* by using second-harmonic generation and two-photon excited fluorescence," *Proc. Natl. Acad. Sci. U.S.A.* **99**, 11014–11019 (2002).
 14. P. Stoller, B. M. Kim, A. M. Rubenchik, K. M. Reiser, and L. B. Da Silva, "Polarizationdependent optical second-harmonic imaging of a rat-tail tendon," *J. Biomed. Opt.* **7**(2), 205–214 (2002).
 15. W. R. Zipfel, R. M. Williams, R. Christie, A. Y. Nikitin, B. T. Hyman, and W. W. Webb, "Live tissue intrinsic emission microscopy using multiphoton-excited native fluorescence and second harmonic generation," *Proc. Natl. Acad. Sci. U.S.A.* **100**, 7075–7080 (2003).
 16. E. Brown, T. Mckee, E. Ditomaso, A. Pluen, B. Seed, Y. Boucher, and R. K. Jain, "Dynamic imaging of collagen and its modulation in tumors *in vivo* using second-harmonic generation," *Nat. Med.* **9**, 796–800 (2003).
 17. G. Cox, E. Kable, A. Jones, I. Fraser, K. Marconi, and M. D. Gorrell, "3-dimensional imaging of collagen using second harmonic generation," *J. Struct. Biol.* **141**, 53–62 (2003).
 18. K. König and I. Riemann, "High-resolution multiphoton tomography of human skin with subcellular spatial resolution and picosecond time resolution," *J. Biomed. Opt.* **8**(3), 432–439 (2003).
 19. A. Zoumi, X. Lu, G. S. Kassab, and B. J. Tromberg, "Imaging coronary artery microstructure using second-harmonic and two-photon fluorescence microscopy," *Biophys. J.* **87**, 2778–2786 (2004).
 20. T. Boulesteix, A. M. Pena, N. Pagès, G. Godeau, M.-P. Sauviat, E. Beaufort, and M. C. Schanne-Klein, "Micrometer scale *ex vivo* multiphoton imaging of unstained arterial wall structure," *Cytometry, Part A* **69A**, 20–26 (2006).
 21. A.-M. Pena, A. Fabre, D. Débarre, J. Marchal-Somme, B. Crestani, J. L. Martin, E. Beaufort, and M. C. Schanne-Klein, "Three-dimensional investigation and scoring of extracellular matrix remodeling during lung fibrosis using multiphoton microscopy," *Microsc. Res. Tech.* **70**, 162–170 (2007).
 22. M. Strupler, A. M. Pena, M. Hernest, P. L. Tharaux, J. L. Martin, E. Beaufort, and M. C. Schanne-Klein, "Second harmonic imaging and scoring of collagen in fibrotic tissues," *Opt. Express* **15**, 4054–4065 (2007).
 23. R. T. A. Megens, S. Reitsma, P. H. M. Schiffers, R. H. P. Hilgers, J. G. R. D. Mey, D. W. Slaaf, M. G. A. O. Egbrink, and M. A. M. J. V. Zandvoort, "Two-photon microscopy of vital murine elastic and muscular arteries. Combined structural and functional imaging with subcellular resolution," *J. Vasc. Res.* **44**, 87–98 (2007).
 24. N. D. Kirkpatrick, S. Andreou, J. B. Hoying, and U. Utzinger, "Live imaging of collagen remodeling during angiogenesis," *Am. J. Physiol. Heart Circ. Physiol.* **292**, H3198–3206 (2007).
 25. M. B. Lilledahl, O. A. Haugen, C. De Lange Davies, and L. O. Svaasand, "Characterization of vulnerable plaques by multiphoton microscopy," *J. Biomed. Opt.* **12**, 044005 (2007).
 26. D. Débarre, W. Suppato, A. M. Pena, A. Fabre, T. Tordjmann, L. Combettes, M. C. Schanne-Klein, and E. Beaufort, "Imaging lipid bodies in cells and tissues using third-harmonic generation microscopy," *Nat. Methods* **3**, 47–53 (2006).
 27. A.-M. Pena, T. Boulesteix, T. Dartigalongue, and M.-C. Schanne-Klein, "Chiroptical effects in the second harmonic signal of collagens I and IV," *J. Am. Chem. Soc.* **127**, 10314–10322 (2005).
 28. S. D. Crowley, S. B. Gurley, M. J. Herrera, P. Ruiz, R. Griffiths, A. P. Kumar, H. S. Kim, O. Smithies, T. H. Le, and T. M. Coffman, "Angiotensin II causes hypertension and cardiac hypertrophy through its receptors in the kidney," *Proc. Natl. Acad. Sci. U.S.A.* **103**, 17985–17990 (2006).
 29. C. M. Lloyd, A. W. Minto, M. E. Dorf, A. Proudfoot, T. N. Wells, D. J. Salant, and J. C. Gutierrez-Ramos, "RANTES and monocyte chemoattractant protein-1 (MCP-1) play an important role in the inflammatory phase of crescentic nephritis, but only MCP-1 is involved in crescent formation and interstitial fibrosis," *J. Exp. Med.* **185**, 1371–1380 (1997).
 30. P. L. Tharaux, C. Chatziantoniou, D. Casellas, L. Fouassier, R. Ardailou, and J. C. Dussaule, "Vascular endothelin-1 gene expression and synthesis and effect on renal type I collagen synthesis and nephroangiosclerosis during nitric oxide synthase inhibition in rats," *Circulation* **99**, 2185–2191 (1999).
 31. R. F. Spurney, P. Y. Fan, P. Ruiz, F. Sanfilippo, D. S. Pisetsky, and T. M. Coffman, "Thromboxane receptor blockade reduces renal injury in murine lupus nephritis," *Kidney Int.* **41**, 973–982 (1992).
 32. M. J. Mulvany, "Small artery remodeling and significance in the development of hypertension," *News Physiol. Sci.* **17**, 105–109 (2002).
 33. E. L. Schiffrin, "Remodeling of resistance arteries in essential hypertension and effects of antihypertensive treatment," *Am. J. Hypertens.* **17**, 1192–1200 (2004).
 34. F. N. Ziyadeh, K. Sharma, M. Ericksen, and G. Wolf, "Stimulation of collagen gene expression and protein synthesis in murine mesangial cells by high glucose is mediated by autocrine activation of transforming growth factor-beta," *J. Clin. Invest.* **93**, 536–542 (1994).
 35. A. Francki, A. D. Bradshaw, J. A. Bassuk, C. C. Howe, W. G. Couser, and E. H. Sage, "SPARC regulates the expression of collagen type I and transforming growth factor-beta1 in mesangial cells," *J. Biol. Chem.* **274**, 32145–32152 (1999).
 36. G. Wolf, U. Haberstroh, and E. G. Neilson, "Angiotensin II stimulates the proliferation and biosynthesis of type I collagen in cultured murine mesangial cells," *Am. J. Pathol.* **140**, 95–107 (1992).
 37. C. Chatziantoniou, J. J. Boffa, R. Ardailou, and J. C. Dussaule, "Nitric oxide inhibition induces early activation of type I collagen gene in renal resistance vessels and glomeruli in transgenic mice. Role of endothelin," *J. Clin. Invest.* **101**, 2780–2789 (1998).
 38. N. Buyukbabani and D. Droz, "Distribution of the extracellular matrix components in human glomerular lesions," *J. Pathol.* **172**, 199–207 (1994).
 39. Y. I. Cai, M. Sich, A. Beziau, M. M. Kleppel, and M. C. Gubler, "Collagen distribution in focal and segmental glomerulosclerosis: an immunofluorescence and ultrastructural immunogold study," *J. Pathol.* **179**, 188–196 (1996).
 40. A. Nerlich and E. Schleicher, "Immunohistochemical localization of extracellular matrix components in human diabetic glomerular lesions," *Am. J. Pathol.* **139**, 889–899 (1991).
 41. A. D. Glick, H. R. Jacobson, and M. A. Haralson, "Mesangial deposition of type I collagen in human glomerulosclerosis," *Hum. Pathol.* **23**, 1373–1379 (1992).
 42. Y. Yang, S. Y. Zhang, M. Sich, A. Beziau, L. P. Van Den Heuvel, and M. C. Gubler, "Glomerular extracellular matrix and growth factors in diffuse mesangial sclerosis," *Pediatr. Nephrol.* **16**, 429–438 (2001).
 43. S. Oparil, M. A. Zaman, and D. A. Calhoun, "Pathogenesis of hypertension," *Ann. Intern. Med.* **139**, 761–776 (2003).